Materials & Design 209 (2021) 109961

Contents lists available at ScienceDirect

Materials & Design

journal homepage: www.elsevier.com/locate/matdes

Toughening mechanisms in V-Si-N coatings

F.F. Ge [a], H.S. Sen [b,*], N. Daghbouj [b,*], M. Callisti [c], Y.J. Feng [a], B.S. Li [d], P. Zhu [a], P. Li [a], F.P. Meng [a], T. Polcar [b], F. Huang [a,*]

[a] Engineering Laboratory of Advanced Energy Materials, Ningbo Institute of Materials Technology and Engineering, Chinese Academy of Sciences, Ningbo, Zhejiang, 315201, China
[b] Department of Control Engineering, Faculty of Electrical Engineering, Czech Technical University in Prague, Technická 2, 160 00 Prague 6, Czechia
[c] Department of Materials Science and Metallurgy, University of Cambridge, 27 Charles Babbage Road, Cambridge CB3 0FS, United Kingdom
[d] State Key Laboratory for Environment-friendly Energy Materials, Southwest University of Science and Technology, Mianyang, Sichuan 621010, China

HIGHLIGHTS

- Super hardness and toughness of VSiN are achieved with Si content at 5.5 at.% Si.
- With Si content, highly textured columnar grains, refined columnar grains, nanocomposite structure are formed.
- DFT revealed that the ternary VSiN coatings become more ductile as the calculated Cauchy pressures (P_C) raise, while the Pugh's ratios (G/B) decrease.
- Transfer of electrons to the Si-N bond from the neighboring V-N bonds causes Friedel oscillations and multiplication of the slip system.

GRAPHICAL ABSTRACT

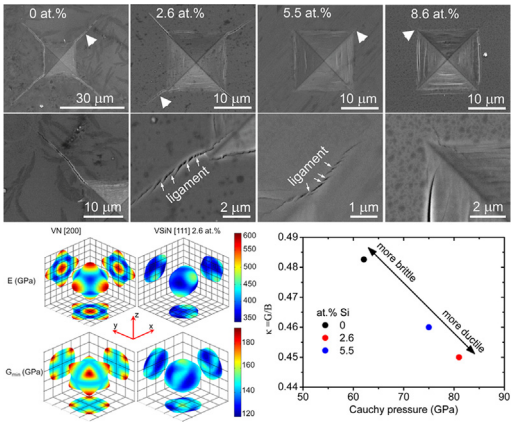

ARTICLE INFO

Article history:
Received 1 April 2021
Revised 28 June 2021
Accepted 5 July 2021
Available online 7 July 2021

Keywords:
Grain boundaries
Toughening mechanisms
Superhard nanocomposite
Physical vapor deposition
Ab initio simulations
Friedel oscillations

ABSTRACT

Microstructural evolution and deformation mechanisms of magnetron sputtered V-Si-N coatings with various Si contents are investigated by transmission electron microscopy, X-ray absorption spectroscopy, and *ab initio* calculations. A small amount of Si atoms was dissolved into the cubic VN lattice, locally reducing the neighboring V-N p-d hybridization near the Si site. The Si content was found to impact the architecture of coating significantly. With increasing Si content, the microstructure evolved through three different architectures: (i) highly textured columnar grains, (ii) refined columnar grains, and (iii) nanocomposite structures where elongated grains were bounded by vein-like boundaries. Enhanced damage tolerance was observed in the nanocomposite structure, where multiple toughening mechanisms become active. *Ab initio* calculations revealed that the incorporation of Si monolayer in the (111)-oriented VN resulted in the formation of weaker Si-N bonds compared to V-N bonds, which allowed a selective response to strain and shear deformations by assisting the activation of the slip systems.

1. Introduction

Many engineering structural materials should be both hard and tough (damage-tolerant) — these requirements are usually inversely related, mainly because changes in materials structure often

* Corresponding authors.
E-mail addresses: senhusey@fel.cvut.cz (H.S. Sen), Nabil.Daghbouj@fjfi.cvut.cz (N. Daghbouj), Huangfeng@nimte.ac.cn (F. Huang).

https://doi.org/10.1016/j.matdes.2021.109961
0264-1275/

affect strength and toughness in very different ways [1,2]. Vanadium nitride (VN) coating is considered one of the most promising candidates for tribological hard coatings and similarly to TiN, it has been widely used as protective coatings due to its excellent mechanical properties [3,4]. VN exhibits a lower friction coefficient than the TiN coatings [4], specifically, when the testing temperature was increased from 773 K to 973 K, the friction coefficient of TiN coating kept a constant of 0.6, while the friction coefficient of VN coating dropped from 0.4 to 0.26 [5]. Physical vapor deposited (PVD) hard ceramic coatings, being intrinsically brittle in most cases, are always subject to catastrophic fracture and low damage tolerance, which can tremendously limit their actual applications. For example, TiSiN superhard coatings fail via brittle transgranular cracking when subjected to uniaxial loads. Although there are several studies in the literature facing the quest for having tough, superhard (H > 40 GPa) coatings, fracture toughness is still of major concern for superhard coatings. Design of hard ceramic coatings with enhanced toughness, which inhibits crack formation or propagation leading to brittle failure during service, is a primary industrial prerequisite [6-8].

Intrinsic toughening mechanisms via valence electron concentration tuning is proposed for hard ceramic coatings, as in the example for alloying cubic nitrides (TiN and VN) with transition metals M = Nb, Ta, Mo, or W [9,10]. However, toughening ceramic materials, in most cases, should be achieved extrinsically by the mechanism of crack-growth toughening. This mechanism primarily operates behind crack tips to lessen the crack-driving force [1,2]. Specifically, extrinsic toughening includes crack deflection and, most importantly, crack bridging. As yet, crack deflection has been the most frequently used toughening mechanism for hard coatings through designing heterogeneous interfaces, i.e. metal/ceramic or ceramic/ceramic multilayers arrangements [8,11-13], and chevron-like columnar boundaries [14]. Although crack bridging is a more effective toughening source than crack deflection [1,2,15] in bulk materials, it is scarcely exploited for hard coatings. It's also known that materials with high interface density or with refined grains (high grain boundary) show high hardness and good toughness [16-23].

In this study, we investigated possible routes of increasing the toughness of V-Si-N coatings fabricated via reactive magnetron sputtering by varying the Si content. The influence of Si content on the microstructure, mechanical properties, and deformation mechanisms of V-Si-N coatings was explored by using various experimental techniques. Finally, *ab initio* calculations were performed to reveal quantum effects on the intrinsic and the extrinsic toughening mechanisms that can potentially contribute to enhance the damage tolerance of V-Si-N hard coatings.

2. Experimental details

The V-Si-N coatings were deposited on Si substrates by reactive magnetron sputtering in a custom-built system that contains two cathodes [24,25]. The right cathode, on which a vanadium target (99.9 at.% in purity) was installed, was driven by a mid-frequency (MF) pulsed-DC power supply (AE Pinnacle Plus + 5/5) at 500 W, 100 kHz, and 80% duty factor. The left cathode, on which a silicon target (99.99 at.% in purity) was installed, was hooked up in parallel to a DC power supply and a radio frequency (RF) power supply (Comdel CV-1000, 81 MHz). The RF power was fixed at 200 W, while the DC power was varied in the range of 0–180 W to adjust the Si content. The total working pressure (Ar + N_2) and the nitrogen partial pressure were 1.0 Pa and 0.30 Pa, respectively. A DC bias voltage of −50 V was applied to the substrate holder. Prior to the deposition, the process chamber was first evacuated to a vacuum better than 5×10^{-5} Pa at room temperature, followed by gradually heating the substrates up to 773 K. We prepared four V-Si-N coatings with various Si contents (0 at.%, 2.6 at.%, 5.5 at.%, and 8.6 at.%). The coating thickness of all samples was 1.1–1.3 μm. The elemental compositions of the coatings that were determined by energy-dispersive x-ray spectroscopy (EDX), are S1 (49.9 at.% V, 0 at.% Si, 49.9 at.% N, 0.2 at.% Ar), S2 (42.5 at.% V, 2.6 at.% Si, 52.7 at.% N, 0.2 at.% Ar), S3 (41.7 at.% V, 5.5 at.% Si, 52.6 at.% N, 0.2 at.% Ar), and S4 (38.7 at.% V, 8.6 at.% Si, 52.5 at.% N, 0.2 at.% Ar). We have estimated the contents of such impurities by means of X-Ray photoelectron spectroscopy (XPS) analysis and found that in our coatings the amount of residual oxygen was negligible [24].

The hardness measurements were conducted by using a nano-indentation system equipped with a diamond Berkovich indenter tip. The maximum indentation depth was set as 150 nm. Residual stress was determined from the substrate curvature method, in which Si(100) pieces, $40 \times 3 \times 0.42$ mm^3 in size, were used. The stress was calculated by the Stoney equation from the curvature change as scanned by a laser beam. Measurement of the V K-edge was carried out at the Shanghai Synchrotron Radiation Facility (SSRF) using the 15 U1 beamlines. The samples were mounted on a holder with motorized (x,y,z) translation and rotation for the incident angle. The measurements were performed in total fluorescence yield (TFY) modes, with the beam size of 200 μm × 200 μm defined by slits. The fluorescence intensity of V Kα1 was recorded by a Si drift detector (Votex, Hitachi USA) with the energy resolution set to 0.5 eV. Both the incident angle and detector angle were typically 45° with respect to the sample surface. Vickers indentation tests were performed on an MVS-1000D1 automatic digital microhardness tester with the normal load of 3 N. A focus ion beam (FIB) workstation (Auriga, Carl Zeiss) was used to prepare the cross-sectional specimens across the indentations. The microstructure of the coatings was characterized by transmission electron microscopy (TEM) on an FEI Tecnai F20 system, a Hitachi S4800 scanning electron microscope (SEM), and an AIST-NT SmartsSPMTM 1000 atomic force microscope (AFM), respectively.

3. DFT modeling

Ab initio calculations in this work were based on density functional theory (DFT) computations, in conjunction with the ultrasoft pseudopotentials, the generalized – gradient approximations (GGA) utilizing the Perdew-Wang (PW91) functional. We used two different supercells due to the change in VN grain orientation from [200] to [111] after the Si addition [24]. For the calculations of VN in which the z-axis was perpendicular to the (200) plane, a supercell with cubic symmetry containing 64 atoms was established by repeating the cubic unit cell of VN 2 × 2 × 2 along the a, b, c directions. For the calculations in which the z-axis was perpendicular to the (111) plane, a supercell with monoclinic symmetry containing 108 atoms was formed where the dimensions were a = b = 8.7 Å and c = 14.11 Å without any Si content. Furthermore, for the calculations with Si content, we simply substituted V atoms in such a way that a (111) Si plane was formed. DFT energy minimization of VN supercells were achieved for the total energy difference between the consecutive electronic steps is below 10^{-5} eV and upon relaxing both the structural parameters and the ion positions until residual forces were lower than 0.01 eV $Å^{-1}$. For the binary VN, the k-points are sampled by a Monkhorst Pack mesh of 7 x 7 x 7, while for the ternary VSiN supercells, the Monkhorst Pack mesh sampling is applied in such a way that the maximum distance between two neighboring k-points are 0.2 $Å^{-1}$. The plane–wave cutoff energy was set to 400 eV. The cut-off energy was increased by 30% to 520 eV for the calculation of elastic con-

stants. Then the *k*-point sampling in each direction was doubled for simulating the density of states.

4. Results

4.1. Bonding evolution with the Si content

X-ray absorption near edge structure (XANES) was employed to resolve changes in the bonding structure of nitride coatings in relation to the chemical composition. Fig. 1 displays the XANES spectra of the vanadium K edge (5450–5500 eV) as a function of Si contents. All spectra showed similar line shapes, where a weak pre-edge peak at ~5467 eV is followed by a broad edge region at 5472–5483 eV, corresponding to a typical shape expected for the NaCl-type structure. Similarly, the XANES spectra at the Ti K-edge of TiSiN coatings also kept a similar line shape as TiN, independent of Si content [26]. It reveals that the additional Si atoms do not modify the lattice structure of V-Si-N. By contrast, in $Ti_{1-x}Al_xN$ coatings, the Ti K-edge XANES spectra vary significantly as a function of the Al content (x), especially for $x > 0.5$, where the Ti atoms are incorporated in the tetrahedral sites of the hexagonal lattice [27].

The pre-edge structures observed in nitrides with NaCl structure are generally ascribed to a $1s \rightarrow 3d$ transition that is partially allowed by the dipolar selection rules due to the mixing of the 3*d* states with the *p* orbitals of the ligand. When the Si content increased from 0 at.% to 5.5 at.%, the pre-edge peak intensity decreased, indicative of a reduction of V-N *p-d* hybridization. According to the subsequent *ab initio* calculations, the V-N *p-d* hybridization was reduced due to the strong interaction between the doped Si atoms and their neighboring N atoms. However, the XANES spectra of the 5.5 at.% and 8.6 at.% coatings nearly overlap, indicating that there might not be a further decrease of the V-N *p-d* hybridization when the Si content increases over 5.5 at.%. Based on the XANES spectra, it was deduced that only a small amount of Si might solubilize in the VN, which would not cause any change of the NaCl-type structure for VN wheras would locally decrease the V-N *p-d* hybridization.

4.2. Microstructural evolution

To investigate the microstructural evolution, symmetric θ-2θ XRD patterns were acquired over 2θ = 36° – 46°. Fig. 2 shows XRD patterns of VN film as a function of Si content where the dashed lines at 37.73° and 43.84° refer to the Bragg angles of (111) and (200) planes of VN monocrystal with the lattice parameter a = 4.13 Å [28], respectively. The diffraction pattern for the as-deposited VN film appeared with one peak at Bragg angles, 2θ = 43.84°, corresponding to (200)VN crystal plane. The crystal structure of the VN coatings remained unchanged with Si addition; all four samples consisted of a (V,Si)N phase having the B1-NaCl cubic structure. No Si_3N_4 phases were detected and a change of preferred orientation was also observed from (200) to (111) as the sample containing 1.2 at.% Si revealed the presence of two peaks at 2θ = 37.42° and θ_B = 43.84° corresponding to (111)VN and (200)VN crystal planes, respectively. When the Si content reached at 2.6 at.%, the (200) peak disappeared completely and the (111) peak shifted toward a lower angle. The increase of Si content to 5.5 at.% did not influence (111) peak shifts. XRD results suggest that the shift of the peaks is caused by Si atoms occupying substitutional sites, which results in a lattice distortion; the position of Si atoms is further discussed in the simulation section below. Expansion (along the film growth direction) of the lattice causes shifts towards $\theta < \theta_B$, while compression causes shifts towards $\theta > \theta_B$ [29-32]. Thus, the shift of (111)VN peak to lower angles indicates an increase in the lattice parameter along the growth direction.

Bright-field (BF) and dark-field (DF) TEM cross-sectional images of the coatings are shown in Fig. 3. The grain size of the coatings decreased as the Si content increases from 0 to 8.6 at.%. For example, binary VN coating exhibited ~ 100 nm wide (200)-oriented columnar grains in agreement with the XRD pattern. The width of the columnar grains decreased to 30 nm with 5.5 at.% Si and to 5 nm with 8.6 at.% Si in ternary V-Si-N coatings. The corresponding selected area electron diffraction (SAED) patterns are shown in Fig. 3a, c, e, and g as insets which were taken with a 0.6 μm aperture centered at the midpoint of the sample. The discrete (200) diffraction spots along the growth direction of the binary sample (0 at.% Si) resulted from large (200)-oriented columns, which was further confirmed by the dark-field image using the

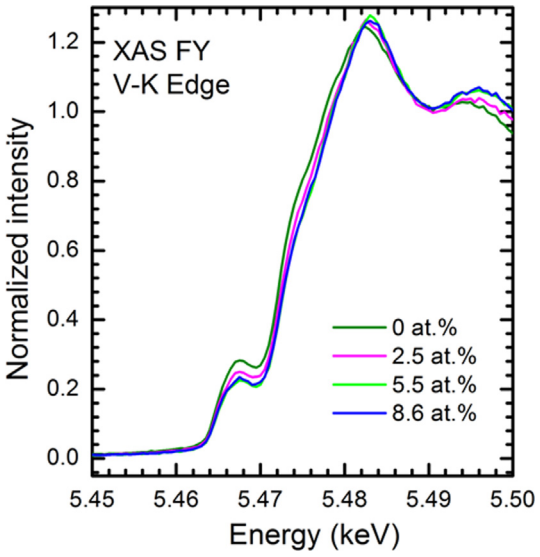

Fig. 1. XANES region of the vanadium K edge as a function of Si content in the coatings.

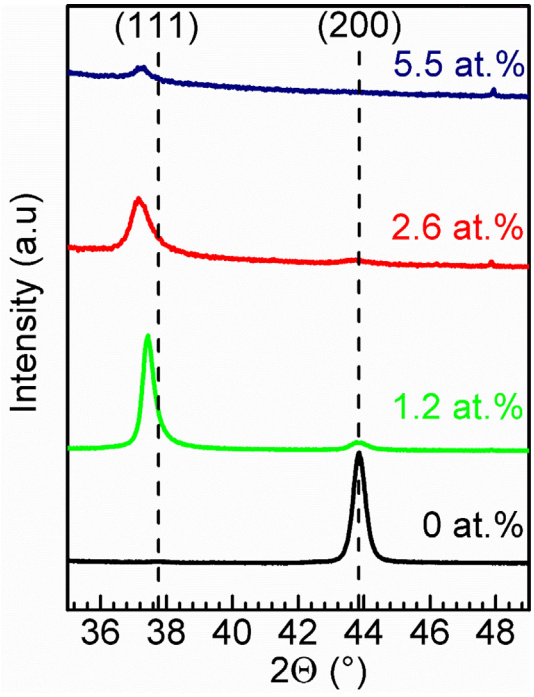

Fig. 2. (a) XRD patterns of VN coatings as a function of Si content. Black dashed lines at 37.73° and 43.84° refer to the Bragg angles of (111) and (200) planes of VN mono-crystal, respectively.

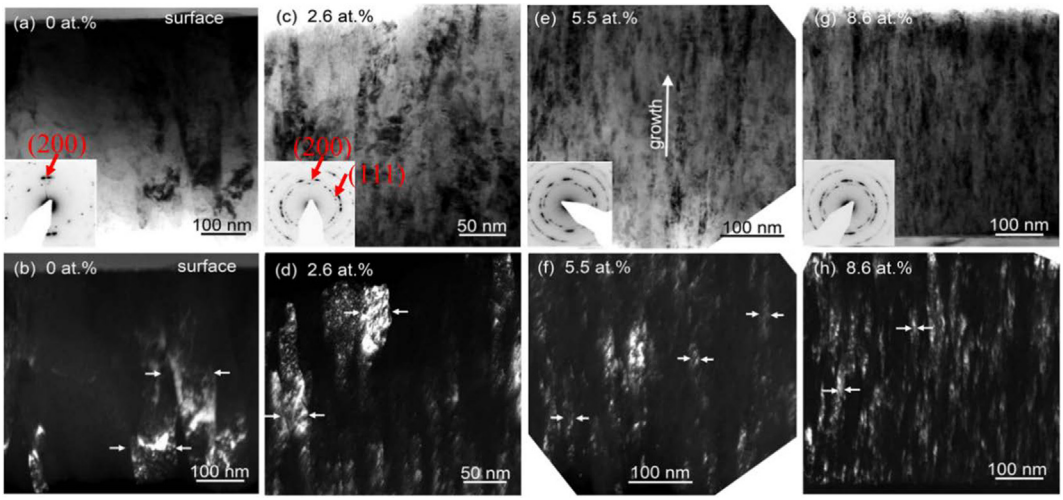

Fig. 3. Cross-sectional TEM images of the VSiN coatings with various Si contents. The bright-field images with Si contents of (a) 0 at%, (c) 2.6 at%, (e) 5.5 at%, (g) 8.6 at% with SAED patterns as insets and the dark-field images with Si content of (b) 0 at%, (d) 2.6 at%, (g) 5.5 at%, (h) 8.6 at%.

(200) diffraction spots (Fig. 3b). This coating exhibited a large and highly oriented columnar structure [33], whereas, with the increase of Si content, the SAED evolved into a series of circular arcs and then rings, an indication of increasing misorientation. The adjacent columns in the 2.6 at.% coating exhibited the orientation of (200) or (111) along the growth direction as shown by SAED in the inset of Fig. 3c. With increasing Si content to 5.5 and 8.6 at.%, the (111) spots become more pronounced, and the rings of (200) did not disappear completely, as suggested by the XRD pattern in Fig. 2. This discrepancy might arise due to the local

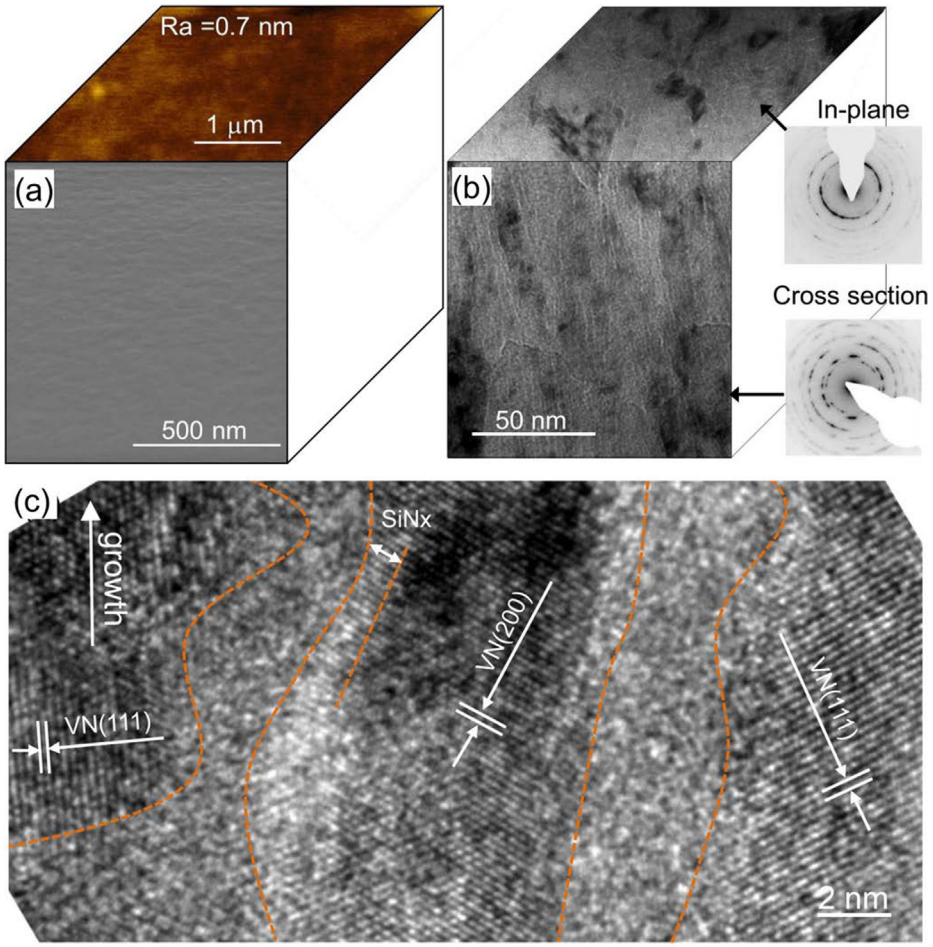

Fig. 4. The microstructural features in multi scales for the 5.5 at.% Si coating. (a) Surface AFM morphology and cross-sectional SEM morphology, (b) In-plane and cross-sectional TEM images, (c) Cross-sectional HRTEM image. In (c), the disorder areas between the VN grains are believed to SiN_x-rich phase.

difference of the small area investigated in SAED to the large area-averaged out by XRD. A nanocomposite structure was further formed in the 5.5Si at.% coating and the 8.6 at.% coatings, where the refined columns or grains are surrounded by SiN_x (in Fig. 4). The thickness of SiN_x layer increases with increasing Si content. Therefore, the addition of Si to the V-N system promotes the VN grains nucleation process that leads to the grain refinement and the formation of a nanocomposite structure (at this range of Si content, the more Si added to the system, the more grain formation, the smaller the grain size).

A detailed microstructural investigation was performed on the 5.5 at.% Si coating, since this coating exhibits the highest hardness and cracks resistance among the studied coatings (see sections *4.3* and *4.4*). Fig. 4a shows a plan view AFM image and a cross-sectional SEM image of the coating. Overall, the coating had a very smooth surface with an average roughness (R_a) of 0.7 nm (AFM), as well as homogeneous and featureless cross-sectional morphology (SEM), where neither columns nor boundaries could be distinguished. A three-dimensional map of the coating was obtained by merging a plan-view and cross-sectional TEM images (see Fig. 4b). Many circular arcs were visible in the cross-sectional selected area diffraction pattern (SADP), whereas the in-plane SADP consisted of a series of rings. Bundles of seemingly bright fibers were sprawling throughout the whole thickness, looking like veins. As precisely identified in Fig. 4c, the elongated VN grains were separated by a thin disordered SiN_x-rich phase with rugged and pore-free interfaces. Therefore, the 5.5 at.% Si coating could be characterized by a column-free and nanocomposite structure that consists of elongated grains adhered with vein-like boundaries. It was different from the nanocolumnar structure of superhard boride coatings, where highly-oriented subcolumns are straightly extending hundreds of nanometers [34,35].

4.3. Evolution of mechanical properties with Si content: Hardness and Young's modulus

The mechanical properties of the coatings measured by nanoindentation are summarized in Table 1. The hardness of the VN coating (~34 GPa) is higher than the single-crystal VN film (14 GPa) [36], but in agreement with that reported for magnetron-sputtered VN coatings [37,38]. The higher hardness in this coating can be attributed to the presence of grain boundaries as the grain size and the hardness generally follows the Hall-Petch relationship [16]. The differences in hardness may also be associated with the variation in the growth structure and internal stress of the coatings compared to the single crystal. After Si addition, the coatings exhibited a hardness > 40 GPa and an indentation modulus E^* > 470 GPa. When the Si concentration increased from 0 to 8.6 at.%, the hardness increase was 43% (from 34 to 48.7 GPa). The 5.5 at.% Si coating exhibited a maximum hardness of ~ 50 GPa and moderate compressive stress of −2.8 GPa. The increase of the hardness can be mainly attributable to the refining of grains and the densifying of growth structure for the addition of Si. It has been revealed in Fig. 4 that the 5.5 at.% Si coating has an exceedingly dense, almost featureless, growth structure, as well as the nanocomposite structure. Meanwhile, both the H/E^* and the H^3/E^{*2} increased when the Si content increased from 0 to 5.5 at.%, and then decreased slightly when the Si content further increased from 5.5 at.% to 8.6 at.%. The highest H/E^* (0.12) and H^3/E^{*2} (0.73) ratios are simultaneously obtained in the 5.5 at.% Si coating. The H/E^* and the H^3/E^{*2} ratios are generally used to characterize resistance against elastic strain to failure and resistance against plastic deformation, respectively [39]. Coatings with higher H/E^* and H^3/E^{*2} ratios usually exhibit enhanced resistance to cracks propagation and wear resistance [40].

Table 1
The mechanical properties and other performance indicators of the VSiN coatings with different Si contents.

Si at.%	0	2.6	5.5	8.6
H (GPa)	34 ± 1	40.1 ± 3.1	50.6 ± 3.1	48.7 ± 2.5
E^* (GPa)	478 ± 32	460 ± 18	423 ± 13	447 ± 15
H/E^*	0.07	0.09	0.12	0.11
H^3/E^{*2} (GPa)	0.17	0.32	0.72	0.58
σ (GPa)	−1.6	−2.5	−2.8	–

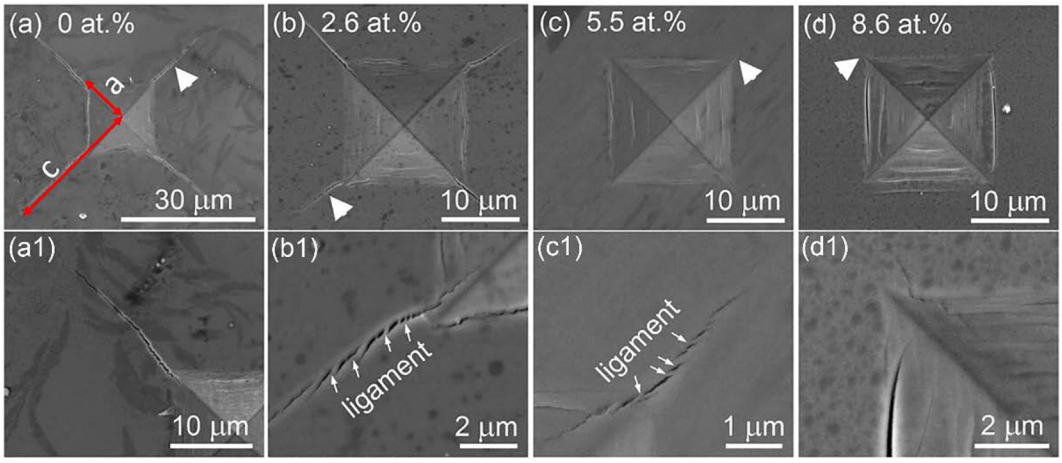

Fig. 5. SEM low magnification images of the Vickers indentation crack patterns on the surfaces of the VSiN coatings with (a) 0 at%, (b) 2.6 at%, (c) 5.5 at% and (d) 8.6 at% Si contents. The crack regions in a, b, c, d pointed by arrows are magnified in a1, b1, c1, d1, respectively. Extrinsic toughening was visible in the 2.6 at.% Si (b1), and the 5.5 at.% Si (c1) coatings.

4.4. Deformation mechanisms

Vickers indentations were made on the surface of all the samples. Fig. 5 displays the lengths and configurations of cracks nucleated at the corners of the indents. The lengths of the radial cracks were 25 μm, 8 μm, and 4 μm for the 0 at.% Si, the 2.6 at.% Si, and the 5.5 at.% Si coatings, respectively. Fracture toughness (K_{IC}) was calculated from the equation proposed by Anstis et al. [41] for half-penny cracks by the following equation:

$$K_{IC} = 0.0154\sqrt{\frac{E}{HV}}\frac{F}{c^{\frac{3}{2}}} \quad (1)$$

where HV is the Vickers microhardness which is deduced from the diagonal length (2a) of the

indentation print and the contact load (F) by the following equation [42]:

$$HV = 1.854\frac{F}{(2a)^2} \quad (2)$$

E is the elastic modulus of the film, (2a) is the diagonal length of the indentation print, F is the contact load and c is the average crack length. The calculated K_{IC} values were 1.62 MPa $m^{1/2}$, 5.22 MPa $m^{1/2}$, and 14.76 MPa $m^{1/2}$ for the three coatings (0 at.%, 2.6 at.% Si, and 5.5 at.%), suggesting that the K_{IC} increases with increasing Si content.

There were no signs of crack bridging and deflecting in the VN coating because the crack propagations presented a relatively straight path (25 μm in length) along [1 1 0] directions around the indents (Fig. 5a) where the corresponding crack image is magnified in Fig. 5a1. The cracks were straightly extending outwards from the corner of the plastic impression, indicative of low crack resistance for the VN coating. Mei *et al.* [36] demonstrated that VN is an inherently brittle material in its stoichiometric single-crystal B1 phase, and the stoichiometric VN phase cleaves in a brittle manner at tensile yield points. Additionally, the columnar structure of the VN coating is also prone to cause an intergranular fracture. However, Fig. 5b and b1 showed that the crack in the 2.6 at.% Si coating was subdivided into several segments by bridging grains with a total length of ~8 μm. The 5.5 at.% Si coating contained very small cracks subdivided into several segments and it had a total length of ~4 μm with deflection and bridging effect during the propagation (crack deflection and bridging) (Fig. 5c and c1). The 2.6 at.% Si and the 5.5 at.% coatings exhibit much higher crack resistance than the VN coating, due to some toughening mechanisms that could dissipate accumulated stress. On the contrary, the 8.6 at.% Si coating failed in an apparently brittle manner in unconstrained loading geometries. Many ring or nest cracks and a large crack-opening displacement were observed in the latter case (Fig. 5d and d1).

Multiple toughening features were particularly exemplified in the 5.5 at.% Si coating. Fig. 6a and 6b present in-plane and cross-sectional micrographs collected around an indentation. A radial crack had initially been deflected, then repeatedly bridged and branched into crack tips. More notably, vertical cracks were also well arrested near the surface, where the ligaments spanned across the cracks to effectively suppress their further opening and growth, although they were produced in a rather catastrophic manner for the brittle fracture of the underneath Si substrate. It has been suggested that the shielding processes at a bridged interface are potentially stronger sources of toughening than the deflection along or across weak interfaces [15]. The crack-bridging frequently proceeds in some natural or bio-inspired bulk materials and structural ceramics, enabling to have a unique combination of high toughness and strength.

Meanwhile, in Fig. 6c, there are many localized shear band patterns on a cross-section, in contrast to sudden and shattered fracture (one dominant shear band) of common ceramics [43-45]. Multiple shear bands are highly favorable to control plastic instability, contributing to a dramatic increase in the plastic strain to failure of the bulk metallic glass (BMG), where each band contributes to the plasticity, and none of the bands carry enough deformation to catastrophic destruction [46,47] These effective toughening mechanisms in the 5.5 at.% Si coating were considered as a key player to its high damage tolerance. The coating retained mild wear in more than 10^5 cycles of sliding in our previous friction-wear tests [25].

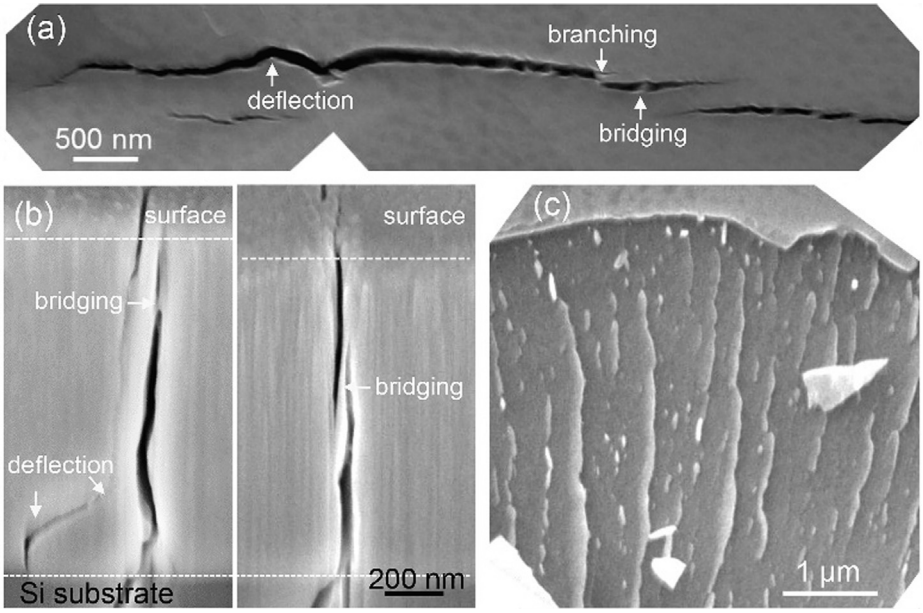

Fig. 6. SEM micrographs of cracks induced by the indentation test in the 5.5 at.% coating, in-plane (a), and cross-section (b), showing multiple extrinsic toughening mechanisms. SEM micrograph of a representative fracture (c), showing a "river-like" feature.

5. Discussion

The results reported in the previous sections showed that Si addition into VN modified the bonding structure and the resulting microstructure of the coatings. A small addition of Si dissolved into VN slightly reduced the V-N p-d hybridization near the Si sites. By increasing the Si content from 0 at.% to 8.6 at.%, the grains changed in size, orientation, and morphology. In fact, the microstructure changed from a highly oriented columnar to a nanocomposite structure for higher Si contents. Specifically, there were two notable microstructural features in the 5.5 at.% Si coating, i.e. the overall column-free and moderately-stressed growth structure, and the elongated grains bounded by vein-like boundaries. Correspondingly, the mechanical properties and the deformation mechanisms changed with structural evolution. Both the mechanical properties and the crack resistance were enhanced for a certain addition of Si. The 5.5 at.% Si coating with the >50 GPa hardness, exhibited limited crack propagation and crack length. Thus, the high crack resistance can sufficiently suppress fracture-dominated wear, which would enhance the service life of the V-Si-N coating in the cutting application and other wear-reduced applications.

5.1. Intrinsic toughening mechanisms

Intrinsic toughening mechanisms are inherent properties of the material, which affect primarily the crack initiation [1,2]. Sangiovanni *et al.* used density functional theory calculations to predict the existence of super toughening in cubic B1 Ti and V ternary nitrides obtained by alloying TiN and VN with Nb, Ta, Mo, and W at 50% concentration [9], which was experimentally proven in $V_{0.5}Mo_{0.5}N$ [48]. Similar mechanical behavior can also be achieved in TiC- and VC-based pseudobinary alloys [10]. The enhanced ductility has been attributed to the formation of stronger metal/metal bonds along the slip direction and weaker metal/N(C) bonds across the slip plane. It is shown that Si atoms generally form planes by replacing Ti/V atoms and bonding with N [49,50]. In order to investigate the electronic origins of this enhanced ductility for the incorporation of Si atoms into VN, we used *ab initio* simulations to study the binary VN for (200) and (111) orientation and the VSiN containing a Si monolayer in (111) orientation with the 2.6 at.%, and 5.5 at.% of Si content, respectively, and the atomic configurations are shown in Fig. 7. The binary VN exhibits a lattice parameter of 4.1 Å which is in accordance with the experimental value obtained by Mei et al [51]. Although VN is a highly anharmonic crystal, which is formed in the B1 structure by lattice vibrations at room temperature [52,53], while dynamically unstable (imaginary phonon frequencies) at 0 K [54,55], with the potential we used, we did not observe any indication of instability such as negative moduli similar to other works that use the same potential [9,56]. To make sure that the instability of the binary VN at 0 K does not interfere with the calculations to contradict the experimental results, we compare the calculated and experimental values of elastic constants below. On the other hand, ternary VSiN with the orientation of SiN along (111) is stable from 0 K till 1400 K [55], making the DFT simulation for the ternary systems reliable.

In light of Fig. 4c and the results of previous works [42,43], we modeled the Si content by replacing a layer of V atoms with Si atoms to form a boundary. We calculated the elastic constants (C_{ij}) for each model, and determined bulk modulus (B), shear modulus (G), Young's modulus (E), Poisson's ratio (v), Pugh's ratio (k), and Cauchy pressure (P_C) from the elastic constants through the Voigt-Reuss-Hill approximations [57-59] using the formulas

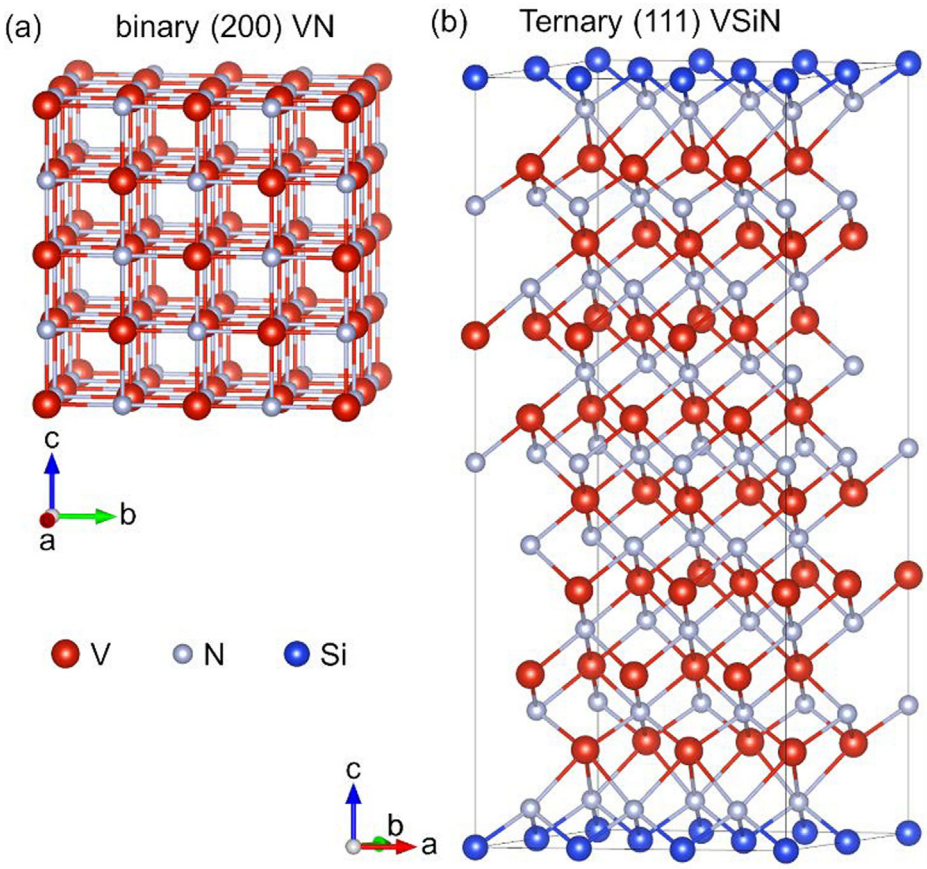

Fig. 7. Atomic configurations used in the simulations: (a) binary (200)VN, (b) ternary (111)VSiN.

Table 2
Calculated Elastic constants C_{ij}, Bulk modulus B, Shear modulus G, and Young's modulus E (in units of GPa) for each VN with different Si contents. Also shown are Poisson's ratio υ and Pugh's ratio k = G/B ratio, Cauchy pressure $P_{C,}$ and Anisotropy index A^u. (* experimental values [63], - calculated from experimental values).

VN (at.% Si)	C_{11}	C_{22}	C_{33}	C_{44}	C_{12}	C_{13}	C_{23}	B	G	E	V	K	P_C	A^u
0-[002]	684	684	684	143	205	205	205	365	176	455	0.29	0.48	62	0.33
	533*			133*	135*			268-	156-	393-	0.26-	0.58-	2-	
0-[111]	563	558	522	246	227	263	262	369	173	453	0.29	0.48	61	0.34
2.6	535	539	535	165	240	240	243	339	153	399	0.30	0.45	81	0.13
5.5	542	530	541	155	186	253	252	332	153	397	0.30	0.46	75	0.13

explained in our previous work [60]. The calculated values for these parameters are summarized in Table 2.

The Pugh's ratio k, i.e. the ratio G/B, is used to qualitatively assess the ductile/brittle behavior of materials. The G/B was proposed by Pugh [61] from a crack-tip dislocation model and by simply assuming that the ratio of bulk modulus B to the shear modulus G reflects the resistance to fracture or plasticity. If the G/B is below a critical value of 0.5–0.6 and its Poisson's ratio υ is above a critical value of 0.25–0.28, the material is predicted to behave in a ductile manner. Otherwise, it is expected to behave in a brittle manner [61]. A decrease of k upon alloying indicates an increased likelihood to improve material's ductility. Additionally, an alternative phenomenological indicator for the ductility of a material is the Cauchy pressure $P_C = C_{12} - C_{44}$ [62], where $P_C < 0$ typically indicates a brittle material and correspondingly $P_C > 0$ suggests a material as ductile. In Table 2, the calculated value (0.29) for the Poisson ratio of binary VN is slightly greater than the experimental one (0.26). In the table, all the values of "υ" are larger than 0.25 which increases to 0.3 after the incorporation of the Si monolayer. This was the first indication that the incorporation of the Si monolayer in the binary VN would cause an enhancement in the ductility. Moreover, based on the values in table 2, the evolution of "k" and P_C of VN as a function of Si content is presented in Fig. 8. The closer to the bottom right corner of the figure (lower k, higher P_C), the higher the ductility of the system. From Fig. 8, one can see that the values of "k" for all binary and ternary systems are less than 0.5 and P_C are positive, implying that they are intrinsically ductile. The incorporation of the Si monolayer decreased the ratio of G/B while increasing the value of P_C, thus showing that the Si incorporation promotes ductility, which is in perfect agreement with the analysis using crack toughness in Section 4.2. Based on the experimental values of Pugh's ratio (just below 0.6) and Cauchy pressure (barely positive), VN is almost behaving in a brittle manner. Although the calculated values of Pugh's ratio and Cauchy pressure of VN indicate a more ductile binary system than the experiment suggests, both experimental and calculated values of Pugh's ratio and Cauchy pressure show that the ternary VSiN is more ductile than the binary VN.

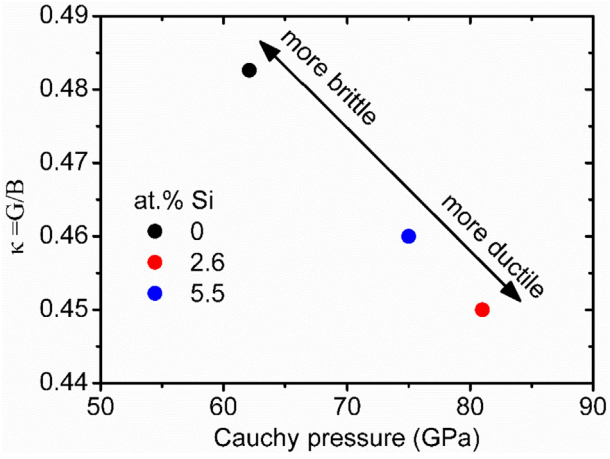

Fig. 8. Evolution of Pugh's ratio and Cauchy pressure of VN system as a function of Si content.

The elastic properties are not only an indicator of the ductile or brittle behavior of a system but also are important for understanding the fundamental properties of materials in engineering applications. Thus, as a potential engineering material, the elastic anisotropy of VN should be studied essentially. The elastic anisotropy of crystals can be revealed by the directional dependence of Young's modulus and shear modulus. The Young's modulus E in general for tensile stress along a direction with a unit vector $\vec{l} = l_1\hat{x} + l_2\hat{y} + l_3\hat{z}$, is given by the following equation (3) [64]

$$\begin{aligned}\frac{1}{E} = {} & S_{11}l_1^4 + S_{22}l_2^4 + S_{33}l_3^4 + (S_{44} + 2S_{23})(l_2l_3)^2 \\ & + (S_{55} + 2S_{13})(l_1l_3)^2 + (S_{66} + 2S_{12})(l_1l_2)^2 \\ & + 2[(S_{14} + S_{56})l_1 + (S_{25} + S_{46})l_2 + (S_{36} + S_{45})l_3]l_1l_2l_3 \\ & + 2\left(S_{24}l_2^3l_3 + S_{34}l_3^3l_2 + S_{15}l_1^3l_2 + S_{35}l_3^3l_1 + S_{16}l_1^3l_2 + S_{26}l_2^3l_1\right) \end{aligned} \quad (3)$$

where S is the compliance. The shear modulus G for the shearing of planes perpendicular to $\vec{l}$ and along a unit vector $\vec{m} = m_1\hat{x} + m_2\hat{y} + m_3\hat{z}$ ($\vec{m}$ is also perpendicular to $\vec{l}$) is given by the following equation (4):

$$\begin{aligned}\frac{1}{G} = {} & 4\{[2S_{12} - (S_{11} + S_{22} - S_{66})]l_1l_2m_1m_2 \\ & + [2S_{23} - (S_{22} + S_{33} - S_{44})]l_2l_3m_2m_3 \\ & + [2S_{13} - (S_{11} + S_{33} - S_{55})]l_1l_3m_1m_3 \\ & + [(S_{16} - S_{36})l_1m_1 + (S_{26} - S_{36})l_2m_2](l_1m_2 + l_2m_1) \\ & + [(S_{24} - S_{14})l_2m_2 + (S_{34} - S_{14})l_3m_3](l_2m_3 + l_3m_2) \\ & + [(S_{35} - S_{25})l_3m_3 + (S_{15} - S_{25})l_1m_1](l_1m_3 + l_3m_1)\} \\ & + S_{44}(l_2m_3 - l_3m_2)^2 + S_{55}(l_3m_1 - l_1m_3)^2 + S_{66}(l_1m_2 - l_2m_1)^2 \\ & + 2[S_{45}(l_2m_3 + l_3m_2)(l_1m_3 + l_3m_1) \\ & + S_{46}(l_2m_3 + l_3m_2)(l_1m_2 + l_2m_1) \\ & + S_{56}(l_1m_3 + l_3m_1)(l_1m_2 + l_2m_1)] \end{aligned} \quad (4)$$

Fig. 8 illustrates three dimensional E and minimum shear modulus G_{min} (it is taken as the minimum value of shear modulus for a shear perpendicular to $\vec{l}$ among all the directions $\vec{m}$) of the VN and the VSiN with 2.6 at.% Si contents, where the z-axis coincides with [200] and [111] directions, and E and G_{min} are projected in the crystal planes. The three-dimensional surface description should be spherical for isotropic crystals. A divergence from the spherical shape can reflect the level of elastic anisotropy. Qualitatively, the projections of binary VN exhibited similar variations in all three planes. On the other hand, the two-dimensional projections of the ternary VSiN were more complicated because of the disturbance in the symmetry due to the introduction of the (111) Si plane. It is obvious that for the binary VN both E and G_{min} did not have a spherical shape (Fig. 9a and Fig. 9c), whereas, with the substitution of Si atoms with V atoms, the shape approached to be spherical (Fig. 9b and Fig. 9d). Moreover, the binary VN had

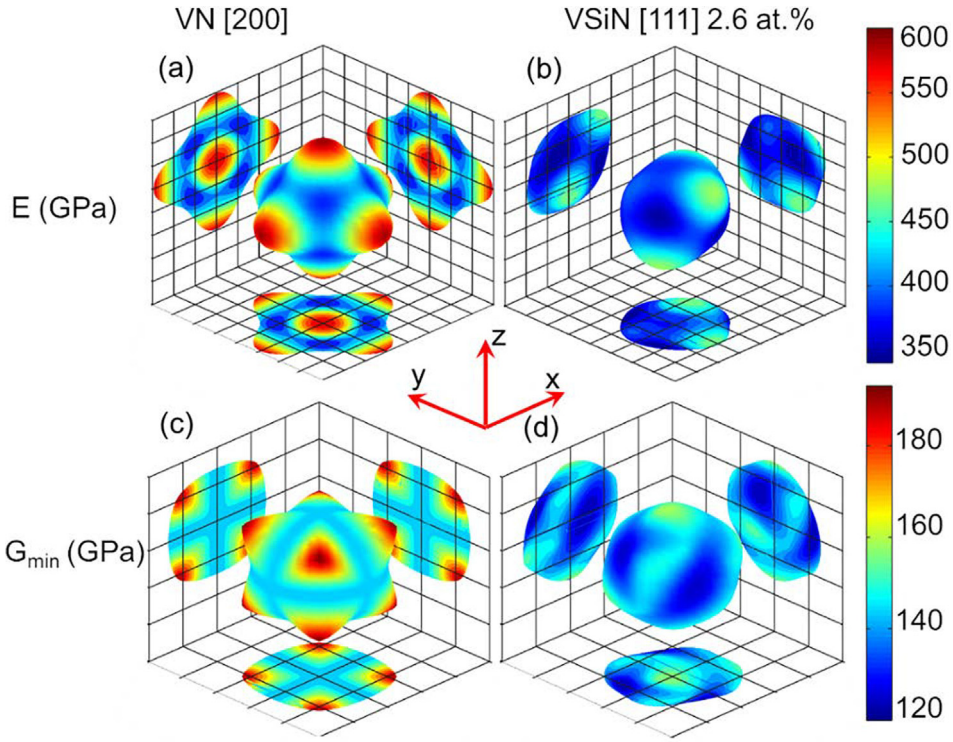

Fig. 9. 3D surface representations of Young's modulus E (a, b) and minimum shear modulus Gmin (c, d) in three dimensions for VN with 0 at.% Si content (a, c) and 2.6 at.% Si content (b, d) where the z-axis coincides with [200] and [111] directions, respectively. The two-dimensional projections are also shown in xy, xz, and yz planes.

more variations of colors in the color maps, suggesting anisotropy similar as in [51]. One can see that the E value varied from 379 GPa to 589 GPa, which accounts for a difference of 55% for the binary VN. By comparison, the maximum E (476 GPa) and the minimum E (347 GPa) values differed by 37% for the VSiN with 2.6 at.% Si content. Therefore, it could be concluded that the binary VN had inherited anisotropy and the incorporation of Si monolayer pushed the coatings to be more isotropic, which is also manifested in the values of A^u presented in Table 2. To be more precise, the anisotropy index can be calculated as $A^u = 5\frac{G_v}{G_r} + \frac{B_v}{B_r} - 6$ [65] where v and r represent the parameters obtained via Voigt [57] and Reuss [58] approximations, respectively. A^u is zero for an isotropic system and increases as the system becomes more anisotropic. The A^u was 0.33 for the binary VN and 0.13 for the VSiN with 2.6 at.% Si, meaning an increase in the isotropy for the incorporation of Si monolayer.

The ternary VSiN with 2.6 at.% Si content had the maximum shear modulus value G_{max} = 200.58 GPa which was obtained for (101) and (−101) planes. The minimum shear modulus G_{min} for the same ternary was attained for (010) plane with the magnitude of 124 GPa, which should have the least resistance to shear. Therefore, it may be concluded that VSiN structure would resist shearing the least in the (010) cleave crystal plane. The fracture toughness can be calculated using the following equation [66]:

$$K_{IC} = V_0^{\frac{1}{6}} G \left(\frac{B}{G}\right)^{\frac{1}{2}} \quad (5)$$

where V_0 is the volume per atom (in m^3), G and B are shear and bulk moduli (in MPa), respectively, and the unit of K_{IC} is in MPa $m^{1/2}$. Using the value of the minimum shear modulus G_{min} of the binary VN (Fig. 9c), the calculated value for the fracture toughness is 3.2 MPa $m^{1/2}$ which is slightly higher than the experimental one of 1.62 MPa $m^{1/2}$. The difference between the predicted and the experimental values also find it in other coatings such as TiN, TiC, and WC [66], which can be related to the use of the bulk modulus instead of the directional Young's modulus in the formula. There is another formula for fracture toughness where the directional Young's modulus is included. In this formula, the fracture toughness is calculated with respect to debonding energy (W_{ad})and the directional Young's modulus (E_{hkl}) using the following equation [67]:

$$K_{IC} = \sqrt{4 W_{ad} E_{hkl}} \quad (6)$$

The debonding energy is calculated through DFT as the difference in total energy per area between the cases where two fracture surfaces are separated and bonding together. The predicted value for the fracture surface (100) and E_{001} is 1.68 MPa $m^{1/2}$ which is very close to the experimental one.

Fig. 10a shows the distances between the atomic planes (and the bond distances) oscillate rapidly around the VN-SiN interface (Friedel oscillations [49]). The oscillations of bond lengths are damped within 10 layers with increasing distance from the SiN interface. The mean interplanar distances of the structure given in Fig. 10a are: 2.045 Å (VN – far-left layer) – (NV) –…– (NV) – …– (VN) – 1.95 Å (NSi - central layer) – 1.95 Å (SiN - central layer) – (NV) –…– (VN) – …– 2.045 Å (VN - far-right layer). The same pattern was reflected in the oscillations of the valence charge-density distributions as is shown in Fig. 10b. This oscillation was the result of valence charge transfer from the metallic VN to the interfacial layer SiN due to a higher electronegativity of Si compared to the transition metal V. This charge transfer increased the bond strength of Si-N while reducing the strength of the neighboring V-N bonds, which would make the pile-up of dislocation harder and give rise to the formation of crack bridges.

To understand the enhanced ductility of the VSiN system with respect to VN in terms of "bonding" and "antibonding" states, we calculated the partial density of states (PDOS) of a V atom in the binary VN (V^b) and the V atoms close (V^c) to and far (V^f) from the Si plane in the VSiN of 5.5 at%.Si (as shown in Fig. 10). The PDOS

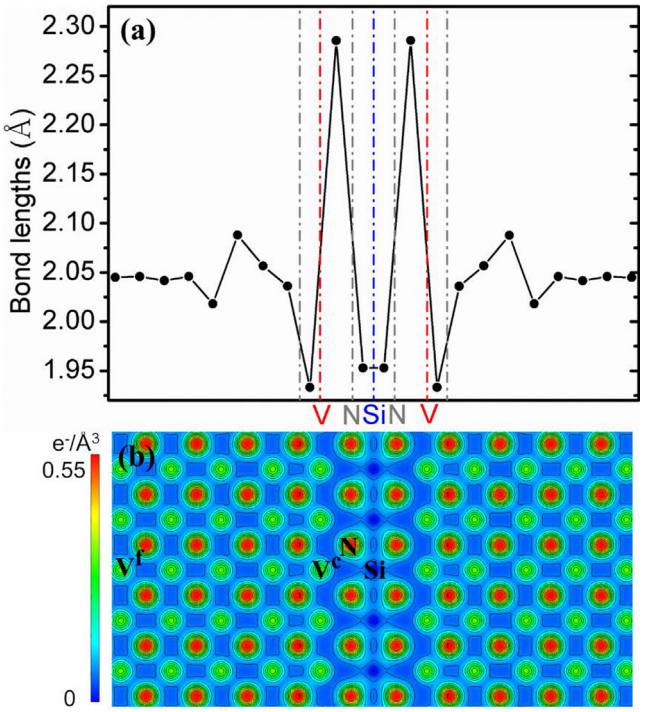

Fig. 10. (a) Bond lengths between atoms in the ternary VSiN around the Si interface, (b) Valance charge density distributions of for the ternary VSiN in (a). The color scale is in e/Å^3.

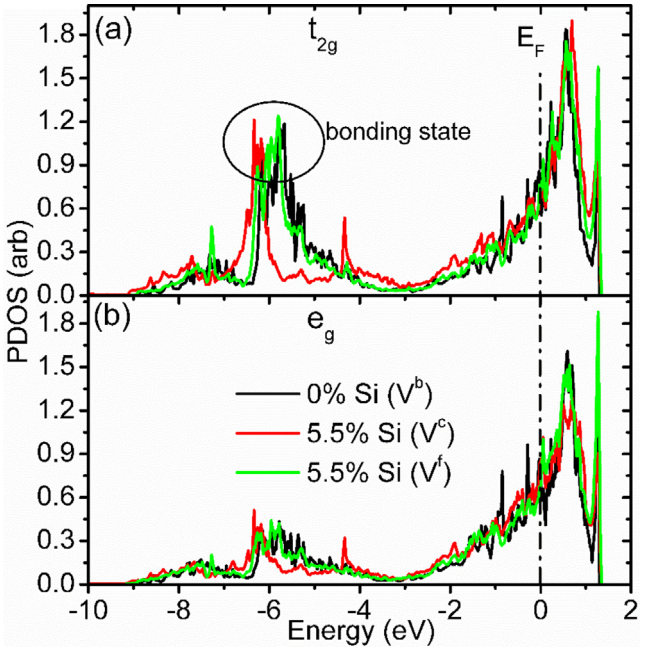

Fig. 11. The density of states for the (a) t_{2g}, (b) e_g state of V atoms in the binary VN (V^b) and in the ternary VSiN (5.5 at.% Si) close to (V^c) and far from (V^f) the Si plane. The Fermi level (E_F) is indicated by a vertical dashed line.

is displayed in Fig. 11a for the t_{2g} state where the bonding state is marked by the circle inset around –6 eV. The occupancy of the bonding state was further calculated by integrating the DOS values over the energy up to the minimum around −3 eV and up to the Fermi level E_f. The V^b and the V^f presented almost similar DOS and the occupancies of the bonding states (~1% difference), whereas the occupancies of the bonding states was lowered by x %, and 11.8% for V^c up to the minimum around −3 eV and up to the Fermi level E_f, respectively. Similarly, the e_g states are plotted in Fig. 11b. The DOS of e_g has the same behavior compared to the DOS of t_{2g}: profile shape, bonding, and anti-bonding states energy windows, and the red-shift of the maximum of bonding state of V^c. The differences of the occupancy of the bonding state of Vc from the ones of Vb and Vf are Y %, and z % up to the minimum around −3 eV and up to the Fermi level E_f, respectively. The lower occupancy means that the V^c – N bonds are weaker compared to the V^b – N bonds, but the V^f – N bonds are as strong as those V^b – N bonds. This weakening of V^c – N bonds would cause easier slip parallel to Si layer, and also was responsible for the reduction of both shear modulus G and bulk modulus B (in Table 2). Although there was an overall decline of the valence electron concentration in the whole VSiN system, the formation of a layered electronic structure could ultimately allow a selective response to strain and shear deformations by assisting the activation of the slip system for dislocation glide. Around this density range, the increase of Si content might result in the multiplication of the slip system for dislocation glide which would enhance the ductility of the coating, as evidenced in our experiments (Fig. 5). This toughening mechanism seems different from that of the alloying of VN with 50 at.% transition metals (Nb, Ta, Mo, and W), where an increase of the valence electron concentrations causes an increase of the bulk modulus B and a decrease of shear modulus G [9,10].

5.2. Extrinsic toughening mechanism

The extrinsic toughness involves microstructural mechanisms that affect only the crack propagation rather than the crack initiation, which is considered as the primary source of toughening for ceramic materials [1,2]. It has been already recognized that heterogeneous microstructures can inhibit various plastic or failure instability mechanisms, including layered aragonite platelets bonded by a thin layer of organic material in natural nacre [68], brick-and-mortar-like architecture in nacre-like alumina ceramics [69], interlocking grains with engineered boundaries in structural ceramics [43], and the *in situ* formed ductile phase dendrite dispersions in the bulk metallic glass BMG [47]. In the case of the 5.5 at.% Si coating, the vein-like boundaries that bond elongated grains could be regarded as a kind of heterogeneous microstructure that would act as a networked self-defense system to manage deformation instability.

The grain bridges are the main mechanism for the greater toughness of most polycrystalline ceramics in comparison to their single-crystal counterparts, and of whisker- and particle-reinforced ceramics [40,50]. The elongated grains in the 5.5 at.% coating could be assumed to give rise to grain bridges since the extent of grain bridges generally increases with grain shape anisotropy. By contrast, it would be less possible that the grain bridges form in the equiaxed grains. The *ab initio* calculation results already suggested that the incorporation of a Si monolayer would result in the multiplication of the slip system for dislocation glide. As a result, to propagate, the crack had to undergo bending or branching. In order to overcome this discontinuity, the bridge-rupture of grains followed these steps; overlap the crack segments, a link between the crack segments, and the rupturing of the bridging grain. These mechanisms needed high mechanical energy, which brings about the deceleration of crack propagation. Comparing Fig. 5a (VN – 0 at.% Si) and Fig. 5c (VSiN – 5.5 at.% Si), it was evident that the latter exhibited small crack lengths that the crack was decomposed into segments, in which the crack segments tended to reach an overlap but had yet not linked up. In return, the crack propagation was hindered by about 5 times (from 21 μm to 4 μm).

Finally, it is a prerequisite for toughening the PVD coatings that a straightly columnar structure and large stress should be avoided firstly. The fracture always prevails in the straight boundaries between columns, such as the 0 at.% Si coating, and even some already refined nanocomposite coatings [70-72] and nano-multilayer coatings [73,74]. Meanwhile, the highly-stressed coatings are usually subjected to catastrophic fracture and low damage tolerance [3,4,75,76]. Ahmed *et al.* have concluded that the fracture mode of TiSiN coatings changes from ductile to brittle when the compressive stress increases from 3.7 GPa to 10.1 GPa [6]. The moderate compressive stress (~2.8 GPa) in the 5.5 at.% Si coating could be expected to increase the critical applied load that causes the fracture of coatings. Thus, it is probable that at high Si content the compressive stress will be large and could make the coating brittle, similarly to other works which show that the crack formation and propagation are dependent on the residual stress [77-80].

6. Conclusion

In summary, the V-Si-N coatings were prepared by reactive magnetron sputtering with a high $T_{deposition}/T_{melting}$ of ~ 0.3 and a low substrate bias voltage (-50 V). The addition of Si could induce multi-scale structural disordering of magnetron sputtered VN coatings, such as densifying the columnar structure, refining the grains, and locally reducing the V-N *p-d* hybridization near the Si sites. Furthermore, the fracture toughness and the deformation mechanism of the coatings strongly depended on their microstructures. It was observed that the columnar coatings failed due to intergranular fracture, and brittle fracture occurred when the amorphous boundary layer became thick. By comparison, the multiple toughening mechanisms, such as crack deflection and crack bridges, were operative in a coating that were characterized by elongated grains separated with extensive vein-like boundaries. We used DFT calculations to show that as compared to the binary VN, the ternary VSiN coatings become more ductile as the calculated Cauchy pressures (P_C) raise, while the Pugh's ratios (G/B) decrease. The SiN layer covering the VN grains would cause the transfer of electrons to the Si-N bond from the neighboring V-N bonds which causes Friedel oscillations and multiplication of the slip system. These results show the possibility of designing multiple toughening mechanisms leading to high levels of damage tolerance for superhard ceramic coatings.

Declaration of Competing Interest

The author declare that there is no conflict of interest.

Acknowledgments

This work was supported by the National Natural Science Foundation (No. 51871231). This study was financially supported by the Czech Science Foundation in the frame of the project 17-17921S and the European Regional Development Fund (project CZ.02.1.01/0.0/0.0/16_019/0000778). Also, this work was supported by the Ministry of Education, Youth and Sports of the Czech Republic through the e-INFRA CZ (ID:90140). M.C. acknowledges Innovate UK (reference number: 113072) for financial support.

Appendix A. Supplementary material

Supplementary data to this article can be found online at https://doi.org/10.1016/j.matdes.2021.109961.

References

[1] R.O. Ritchie, The conflicts between strength and toughness, Nat. Mater. 10 (2011) 817–822, https://doi.org/10.1038/nmat3115.
[2] M.E. Launey, R.O. Ritchie, On the fracture toughness of advanced materials, Adv. Mater. 21 (2009) 2103–2110, https://doi.org/10.1002/adma.200803322.
[3] R. Ali, M. Sebastiani, E. Bemporad, Influence of Ti–TiN multilayer PVD-coatings design on residual stresses and adhesion, Mater. Des. 75 (2015) 47–56, https://doi.org/10.1016/j.matdes.2015.03.007.
[4] N. Fateh, G.A. Fontalvo, G. Gassner, C. Mitterer, Influence of high-temperature oxide formation on the tribological behaviour of TiN and VN coatings, Wear 262 (2007) 1152–1158, https://doi.org/10.1016/j.wear.2006.11.006.
[5] R. Franz, C. Mitterer, Vanadium containing self-adaptive low-friction hard coatings for high-temperature applications: a review, Surf. Coat. Technol. 228 (2013) 1–13, https://doi.org/10.1016/j.surfcoat.2013.04.034.
[6] M.S. Ahmed, Z. Zhou, P. Munroe, L.K.Y. Li, Z. Xie, Control of the damage resistance of nanocomposite TiSiN coatings on steels: Roles of residual stress, Thin Solid Films 519 (2011) 5007–5012, https://doi.org/10.1016/j.tsf.2011.01.070.
[7] M.S. Ahmed, P. Munroe, Z.-T. Jiang, X. Zhao, M. Wajrak, H. Guo, W. Rickard, Z. Xie, Corrosion- and damage-resistant nitride coatings for steel, J. Am. Ceram. Soc. 95 (2012) 2997–3004, https://doi.org/10.1111/j.1551-2916.2012.05328.x.
[8] P.C. Wo, X.L. Zhao, P.R. Munroe, Z.F. Zhou, K.Y. Li, D. Habibi, Z.H. Xie, Extremely hard, damage-tolerant ceramic coatings with functionally graded, periodically varying architecture, Acta Mater. 61 (2013) 193–204, https://doi.org/10.1016/j.actamat.2012.09.049.
[9] D.G. Sangiovanni, L. Hultman, V. Chirita, Supertoughening in B1 transition metal nitride alloys by increased valence electron concentration, Acta Mater. 59 (2011) 2121–2134, https://doi.org/10.1016/j.actamat.2010.12.013.
[10] D. Edström, D.G. Sangiovanni, L. Hultman, I. Petrov, J.E. Greene, V. Chirita, Elastic properties and plastic deformation of TiC- and VC-based pseudobinary alloys, Acta Mater. 144 (2018) 376–385, https://doi.org/10.1016/j.actamat.2017.10.047.
[11] P. Wieciński, J. Smolik, H. Garbacz, K.J. Kurzydłowski, Failure and deformation mechanisms during indentation in nanostructured Cr/CrN multilayer coatings, Surf. Coatings Technol. 240 (2014) 23–31, https://doi.org/10.1016/j.surfcoat.2013.12.006.
[12] M. Schlögl, C. Kirchlechner, J. Paulitsch, J. Keckes, P.H. Mayrhofer, Effects of structure and interfaces on fracture toughness of CrN/AlN multilayer coatings, Scr. Mater. 68 (2013) 917–920, https://doi.org/10.1016/j.scriptamat.2013.01.039.
[13] R. Daniel, M. Meindlhumer, J. Zalesak, B. Sartory, A. Zeilinger, C. Mitterer, J. Keckes, Fracture toughness enhancement of brittle nanostructured materials by spatial heterogeneity: a micromechanical proof for CrN/Cr and TiN/SiOx multilayers, Mater. Des. 104 (2016) 227–234, https://doi.org/10.1016/j.matdes.2016.05.029.
[14] R. Daniel, M. Meindlhumer, W. Baumegger, J. Zalesak, B. Sartory, M. Burghammer, C. Mitterer, J. Keckes, Grain boundary design of thin films: Using tilted brittle interfaces for multiple crack deflection toughening, Acta Mater. 122 (2017) 130–137, https://doi.org/10.1016/j.actamat.2016.09.027.
[15] B.R. Lawn, Fracture of brittle solids, Cambridge University Press, New York, 2004.
[16] A. Misra, J.P. Hirth, R.G. Hoagland, Length-scale-dependent deformation mechanisms in incoherent metallic multilayered composites, Acta Mater. 53 (2005) 4817–4824, https://doi.org/10.1016/j.actamat.2005.06.025.
[17] M. Callisti, T. Polcar, Combined size and texture-dependent deformation and strengthening mechanisms in Zr/Nb nano-multilayers, Acta Mater. 124 (2017) 247–260, https://doi.org/10.1016/j.actamat.2016.11.007.
[18] N. Daghbouj, M. Callisti, H. S. Sen a, M. Karlik, J. Cech, M. Vronka, V. Havránek, J. Capek, P. Minárik, P. Bábor, T. Polcar, Interphase boundary layer-dominated strain mechanisms in Cu+ implanted Zr-Nb nanoscale multilayers, Acta Mater. 202, (2021) 317–330. https://doi.org/10.1016/j.actamat.2020.10.072.
[19] H. Jiang, X. Wang, I. Szlufarska, The multiple roles of small angle tilt grain boundaries in annihilating radiation damage in SiC, scientific reports 7 (2017) 42358. https://doi.org/10.1038/srep42358.
[20] M. Meindlhumer, L.R. Brandt, J. Zalesak, M. Rosenthal, H. Hruby, J. Kopecek, E. Salvati, C. Mitterer, R. Daniel, J. Todt, J. Keckes, A.M. Korsunsky, Evolution of stress fields during crack growth and arrest in a brittle-ductile CrN-Cr clamped-cantilever analysed by X-ray nanodiffraction and modelling, Mater. Des. 198 (2021), https://doi.org/10.1016/j.matdes.2020.109365 109365.
[21] T. Inoue, R. Ueji, Improvement of strength, toughness and ductility in ultrafine-grained low-carbon steel processed by warm bi-axial rolling, Mater. Sci. Eng., A 786 (2020), https://doi.org/10.1016/j.msea.2020.139415 139415.
[22] J.Y. Wu, B. Wang, B.X. Wang, R.D.K. Misra, Z.D. Wang, Toughness and ductility improvement of heavy EH47 plate with grain refinement through inter-pass cooling, Mater. Sci. Eng., A 733 (2018) 117–127, https://doi.org/10.1016/j.msea.2018.07.001.
[23] J. Ast, M. Ghidelli, K. Durst, M. Göken, M. Sebastiani, A.M. Korsunsky, A review of experimental approaches to fracture toughness evaluation at the micro-scale, Mater. Des. 173 (2019), https://doi.org/10.1016/j.matdes.2019.107762 107762.
[24] F. Huang, F. Ge, P. Zhu, H. Wang, F. Meng, S. Li, Superhard V-Si-N coatings (>50GPa) with the cell-like nanostructure prepared by magnetron sputtering, Surf. Coatings Technol. 232 (2013) 600–605, https://doi.org/10.1016/j.surfcoat.2013.06.035.

[25] F. Ge, P. Zhu, F. Meng, F. Huang, Enhancing the wear resistance of magnetron sputtered VN coating by Si addition, Wear 354–355 (2016) 32–40, https://doi.org/10.1016/j.wear.2016.01.001.
[26] J.L. Endrino, S. Palacín, A. Gutiérrez, F. Schäffers, J.E. Krzanowski, Low and increased solubility of silicon in metal nitrides: evidence by X-ray absorption near edge structure, J. Mater. Sci. 42 (2007) 7607–7610, https://doi.org/10.1007/s10853-007-1870-9.
[27] J. L. Endrino, C. Arhammar, A. Gutierrez, R. Gago, D. Horwat, L. Soriano, G. Fox-Rabinovich, D. Martın y Marero, J. Guo, J.-E. Rubensson, J. Andersson, Spectral evidence of spinodal decomposition, phase transformation and molecular nitrogen formation in supersaturated TiAlN films upon annealing, Acta Materialia 59 (2011) 6287–6296. http://dx.doi.org/10.1016/j.actamat.2011.06.039.
[28] P. Lazar, J. Redinger, Density functional theory applied to VN/TiN multilayers, Phy Rev B 76 (2007), https://doi.org/10.1103/PhysRevB.76.174112 174112.
[29] N. Daghbouj, B.S. Li, M. Callisti, H.S. Sen, M. Karlik, T. Polcar, Microstructural evolution of helium-implanted 6H-SiC subjected to different irradiation conditions and annealing temperatures: a multiple characterization study, Acta Mater. 181 (2019) 160–172, https://doi.org/10.1016/j.actamat.2019.09.027.
[30] N. Daghbouj, B.S. Li, M. Callisti, H.S. Sen, J. Lin, X. Ou, M. Karlik, T. Polcar, The structural evolution of light-ion implanted 6H-SiC single crystal: comparison of the effect of helium and hydrogen, Acta Mater. 188 (2020) 609–622, https://doi.org/10.1016/j.actamat.2020.02.046.
[31] N. Daghbouj, N. Cherkashin, F.-X. Darras, V. Paillard, M. Fnaiech, A. Claverie, Effect of the order of He^+ and H^+ ion co-implantation on damage generation and thermal evolution of complexes, platelets, and blisters in silicon, J. Appl. Phys. 119 (2016), https://doi.org/10.1063/1.4945032 135308.
[32] N. Daghbouj, B.S. Li, M. Karlik, A. Declemy, 6H-SiC blistering efficiency as a function of the hydrogen implantation fluence, Appl. surf. Sci. 466 (2019) 141, https://doi.org/10.1016/j.apsusc.2018.10.005.
[33] F. Ge, P. Zhu, F. Meng, Q. Xue, F. Huang, Achieving very low wear rates in binary transition-metal nitrides: the case of magnetron sputtered dense and highly oriented VN coatings, Surf. Coatings Technol. 248 (2014) 81–90, https://doi.org/10.1016/j.surfcoat.2014.03.035.
[34] P.H. Mayrhofer, C. Mitterer, J.G. Wen, J.E. Greene, I. Petrov, Self-organized nanocolumnar structure in superhard TiB2 thin films, Appl. Phys. Lett. 86 (2005), https://doi.org/10.1063/1.1887824 131909.
[35] M. Audronis, A. Leyland, P.J. Kelly, A. Matthews, The effect of pulsed magnetron sputtering on the structure and mechanical properties of CrB2 coatings, Surf. Coatings Technol. 201 (2006) 3970–3976, https://doi.org/10.1016/j.surfcoat.2006.08.006.
[36] A.B. Mei, H. Kindlund, E. Broitman, L. Hultman, I. Petrov, J.E. Greene, D.G. Sangiovanni, Adaptive hard and tough mechanical response in single-crystal B1 VNx ceramics via control of anion vacancies, Acta Mater. 192 (2020) 78, https://doi.org/10.1016/j.actamat.2020.03.037.
[37] J.-K. Park, Y.-J. Baik, Increase of hardness and oxidation resistance of VN coating by nanoscale multilayered structurization with AlN, Mater. Lett. 62 (2008) 2528–2530, https://doi.org/10.1016/j.matlet.2007.12.040.
[38] G. Farges, E. Beauprez, D. Degout, Preparation and characterization of V-N films deposited by reactive triode magnetron sputtering, Surf. Coat. Technol. 54 (55) (1992) 115–120.
[39] M. Mikula, M. Truchlý, D.G. Sangiovanni, D. Plašienka, T. Roch, M. Gregor, P. Ďurina, M. Janík, P. Kúš, Experimental and computational studies on toughness enhancement in Ti-Al-Ta-N quaternaries, J. Vac. Sci. Technol. A Vacuum, Surfaces, Film. 35 (2017), https://doi.org/10.1116/1.4997431 060602.
[40] L. Aissani, A. Alhussein, C. Nouveau, L. Radjehi, I. Lakdhar, E. Zgheib, Evolution of microstructure, mechanical and tribological properties of vanadium carbonitride coatings sputtered at different nitrogen partial pressures, Surf. Coatings Technol. 374 (2019) 531–540, https://doi.org/10.1016/j.surfcoat.2019.06.034.
[41] G.R. Anstis, P. Chantikul, B.R. Lawn, D.B. Marshall, A critical evaluation of indentation techniques for measuring fracture toughness: I, direct crack measurements, J. Am. Ceram. Soc. 64 (1981) 533–538, https://doi.org/10.1111/j.1151-2916.1981.tb10320.x.
[42] F.A. McClintock, A.S. Argon, Mechanical behaviour of materials, Addison Wesley Publishing Company, Massachussets, USA, 1966.
[43] Y. Waku, N. Nakagawa, T. Wakamoto, H. Ohtsubo, K. Shimizu, Y. Kohtoku, A ductile ceramic eutectic composite with high strength at 1,873 K, Nature 389 (1997) 49–52, https://doi.org/10.1038/37937.
[44] A.R. Studart, Turning brittleness into toughness, Nat. Mater. 13 (2014) 433–435, https://doi.org/10.1038/nmat3955.
[45] E. Munch, M. E. Launey, D. H. Alsem, E. Saiz, A. P. Tomsia, R. O. Ritchie, Tough, bio-inspired hybrid materials, Science (80-) 322 (2008) 1516–1520. DOI: 10.1126/science.1164865
[46] E. Ma, Controlling plastic instability, Nat. Mater. 2 (2003) 7–8, https://doi.org/10.1038/nmat797.
[47] C.C. Hays, C.P. Kim, W.L. Johnson, Microstructure controlled shear band pattern formation and enhanced plasticity of bulk mmetallic glasses containing in situ formed ductile phase dendrite dispersions, Phys. Rev. Lett. 84 (2000) 2901–2904, https://doi.org/10.1103/PhysRevLett.84.2901.
[48] H. Kindlund, D.G. Sangiovanni, L. Martínez-de-Olcoz, J. Lu, J. Jensen, J. Birch, I. Petrov, J.E. Greene, V. Chirita, L. Hultman, Toughness enhancement in hard ceramic thin films by alloy design, APL Mater. 1 (2013), https://doi.org/10.1063/1.4822440 042104.
[49] R.F. Zhang, A.S. Argon, S. Veprek, Friedel oscillations are limiting the strength of superhard nanocomposites and heterostructures, Phys. Rev. Lett. 102 (2009), https://doi.org/10.1103/PhysRevLett.102.015503 015503.
[50] S. Veprek, M.G.J. Veprek-Heijman, The formation and role of interfaces in superhard nc-MenN/a-Si3N4 nanocomposites, Surf. Coatings Technol. 201 (2007) 6064–6070, https://doi.org/10.1016/j.surfcoat.2006.08.112.
[51] A.B. Mei, M. Tuteja, D.G. Sangiovanni, R.T. Haasch, A. Rockett, L. Hultman, I. Petrova, J.E. Greene, Growth, nanostructure, and optical properties of epitaxial VNx/MgO(001) (0.80 r x r 1.00) layers deposited by reactive magnetron sputtering, J. Mater. Chem. C 4 (2016) 7924, https://doi.org/10.1039/c6tc02289h.
[52] F. Kubel, W. Lengauer, K. Yvon, Structural phase-transition at 205-K in stoichiometric vanadium nitride, Physical Review B 38 (1988) 12908.
[53] A.B. Mei, O. Hellman, N. Wireklint, C.M. Schleputz, D.G. Sangiovanni, B. Alling, A. Rockett, L. Hultman, I. Petrov, J.E. Greene, Dynamic and structural stability of cubic vanadium nitride, PRB 91 (2015), https://doi.org/10.1103/PhysRevB.91.054101 054101.
[54] E.I. Isaev, S.I. Simak, I.A. Abrikosov, R. Ahuja, Yu.Kh. Vekilov, M.I. Katsnelson, A. I. Lichtenstein, B. Johansson, Phonon related properties of transition metals, their carbides, and nitrides: a first-principles study, J. Appl. Phys. 101 (2007), https://doi.org/10.1063/1.2747230 123519.
[55] V.I. Ivashchenko, S. Veprek, P.E.A. Turchi, V.I. Shevchenko, Comparative first-principles study of TiN/SiNx/TiN interfaces, PRB 85 (2012), https://doi.org/10.1103/PhysRevB.85.195403 195403.
[56] D.G. Sangiovanni, V. Chirita, L. Hultman, Electronic mechanism for toughness enhancement in TixM1−xN (M=Mo and W), PRB 81 (2010), https://doi.org/10.1103/PhysRevB.81.104107 104107.
[57] W. Voigt, Lehrbuch der kristallphysik (mit ausschluss der kristalloptik). B. G. Teubners Sammlung von Lehrbuchern auf dem Gebiete der mathematischen Wissenschaften mit Einschluss ihrer Anwendungen, bd. xxxiv, B. G. Teubner, Leipzig, Berlin (1928).
[58] A. Reuss, Berechnung der fliegrenze von mischkristallen auf grund der plastizittsbedingung für einkristalle, ZAMM - J. Appl. Math. Mech./Z. Angew. Math. Mech. 9 (1929) 49–58.
[59] R. Hill, The elastic behaviour of a crystalline aggregate, Proc. Phys. Soc. 65 (1952) 349–354, https://doi.org/10.1088/0370-1298/65/5/307.
[60] H.S. Sen, T. Polcar, Vacancy-interface-helium interaction in Zr-Nb multi-layer system: A first-principles study, J. Nucl. Mater. 518 (2019) 11–20, https://doi.org/10.1016/j.jnucmat.2019.02.030.
[61] S.F. Pugh, Relations between the elastic moduli and the plastic properties of polycrystalline pure metals, Philos. Mag. Ser. 45 (1954) 823–843, https://doi.org/10.1080/14786440808520496.
[62] D.G. Pettifor, Theoretical predictions of structure and related properties of intermetallics, Mater. Sci. Technol. 8 (1992) 345–349, https://doi.org/10.1179/mst.1992.8.4.345.
[63] J.O. Kim, J.D. Achenbach, P.B. Mirkarimi, M. Shinn, S.A. Barnett, Elastic constants of single crystal transition metal nitride films measured by linefocus acoustic microscopy, J. Appl. Phys. 72 (1992) 1805, https://doi.org/10.1063/1.351651.
[64] T.C.T. Ting, On anisotropic elastic materials for which Young's Modulus E(n) is independent of n or the Shear Modulus G(n, m) is independent of n and m, J. Elast. 81 (2006) 271–292, https://doi.org/10.1007/s10659-005-9016-2.
[65] S.I. Ranganathan, M. Ostoja-Starzewski, Universal elastic anisotropy index, Phys. Rev. Lett. 101 (2008), https://doi.org/10.1103/PhysRevLett.101.055504 055504.
[66] H. Niu, Sh. Niu, A.R. Oganov, Simple and accurate model of fracture toughness of solids, J. Appl. Phys. 125 (2019), https://doi.org/10.1063/1.5066311 065105.
[67] M. Bielawski, K. Chen, Computational evaluation of adhesion and mechanical properties of nanolayered erosion-resistant coatings for gas turbines, J. Eng. Gas Turbines Power 133 (2011) 042102–042103, https://doi.org/10.1115/1.4002158.
[68] M.A. Meyers, P.-Y. Chen, A.Y.-M. Lin, Y. Seki, Biological materials: Structure and mechanical properties, Prog. Mater. Sci. 53 (2008) 1–206, https://doi.org/10.1016/j.pmatsci.2007.05.002.
[69] S. Deville, Freeze-casting of porous ceramics: a review of current achievements and issues, Adv. Eng. Mater. 10 (2008) 155–169, https://doi.org/10.1002/adem.200700270.
[70] C.J. Gilbert, J.J. Cao, L.C. Jonghe, R.O. Ritchie, Crack-growth resistance-curve behavior in silicon carbide: small versus long cracks, J. Am. Ceram. Soc. 80 (2005) 2253–2261, https://doi.org/10.1111/j.1151-2916.1997.tb03115.x.
[71] M. Stueber, H. Holleck, H. Leiste, K. Seemann, S. Ulrich, C. Ziebert, Concepts for the design of advanced nanoscale PVD multilayer protective thin films, J. Alloys Compd. 483 (2009) 321–333, https://doi.org/10.1016/j.jallcom.2008.08.133.
[72] A. Furlan, J. Lu, L. Hultman, U. Jansson, Control of crystallinity in sputtered Cr–Ti–C films, Acta Mater. 61 (2013) 6352–6361, https://doi.org/10.1016/j.actamat.2013.06.045.
[73] I. Povstugar, P. Choi, D. Tytko, J. Ahn, D. Raabe, Interface-directed spinodal decomposition in TiAlN / CrN multilayer hard coatings studied by atom probe tomography, Acta Mater. 61 (2013) 7534–7542, https://doi.org/10.1016/j.actamat.2013.08.028.

[74] P.Eh. Hovsepian, D.B. Lewis, W.-D. Münz, Recent progress in large scale manufacturing of multilayer superlattice hard coatings, Surf. Coat. Technol. 133–134 (2000) 166–175, https://doi.org/10.1016/S0257-8972(00)00959-2.
[75] D.B. Lewis, P.E. Hovsepian, C. Schönjahn, A. Ehiasarian, I.J. Smith, Industrial scale manufactured superlattice hard PVD coatings, Surf. Eng. 17 (2001) 15–27, https://doi.org/10.1179/026708401101517557.
[76] K. Sato, N. Ichimiya, A. Kondo, Y. Tanaka, Microstructure and mechanical properties of cathodic arc ion-plated (Al, Ti)N coatings, Surf. Coatings Technol. 163–164 (2003) 135–143, https://doi.org/10.1016/S0257-8972(02)00610-2.
[77] X. Song, S. Feih, W. Zhai, C.-N. Sun, F. Li, R. Maiti, J. Wei, Y. Yang, V. Oancea, L.R. Brandt, A.M. Korsunsky, Advances in additive manufacturing process simulation: Residual stresses and distortion predictions in complex metallic components, Mater. Des. 193 (2020), https://doi.org/10.1016/j.matdes.2020.108779 108779.
[78] E. Salvati, H. Zhang, K. S. Fong, X. Song, A. M. Korsunsky, Separating plasticity-induced closure and residual stress contributions to fatigue crack retardation following an overload, Journal of the Mechanics and Physics of Solids 98, (20016) 222-235. https://doi.org/10.1016/j.jmps.2016.10.001
[79] L.R. Brandt, E. Salvati, C. Papadaki, H. Zhang, S. Ying, E. Le Bourhis, I. Dolbnya, T. Sui, A.M. Korsunsky, Probing the deformation and fracture properties of Cu/W nano-multilayers by in situ SEM and synchrotron XRD strain microscopy, Surf. Coat. Technol. 320 (2017) 158–167, https://doi.org/10.1016/j.surfcoat.2017.01.065.
[80] J.P. Belnoue, T.-S. Jun, F. Hofmann, B. Abbey, A.M. Korsunsky, Evaluation of the overload effect on fatigue crack growth with the help of synchrotron XRD strain mapping, Eng. Fract. Mech. 77 (2010) 3216–32263217, https://doi.org/10.1016/j.engfracmech.2010.08.018.